

A Search for Gravitationally Lensed Quasars in Pan-STARRS1: Spectroscopy and Sources of Shear in the Diamond 2M1134–2103

Cristian E. Rusu,^{1*} Ciprian T. Berghea,² Christopher D. Fassnacht,³
Anupreet More,⁴ Erica Seman² and George J. Nelson²

¹*Subaru Telescope, National Astronomical Observatory of Japan, 650 N Aohoku Pl, Hilo, HI 96720*

²*U.S. Naval Observatory (USNO), 3450 Massachusetts Avenue NW, Washington, DC 20392, USA*

³*Department of Physics, University of California, Davis, CA 95616, USA*

⁴*Kavli IPMU (WPI), UTIAS, The University of Tokyo, Kashiwa, Chiba 277-8583, Japan*

Accepted XXX. Received YYY; in original form ZZZ

ABSTRACT

We present results of a systematic search for gravitationally lensed quasars in Pan-STARRS1. Our final sample of candidates comprise of 46 new doubles, 2 new quads, and 6 known lenses, which we discovered independently. In the absence of spectroscopy to verify the lensing nature of the candidates, the main sources of contaminants are likely to be quasar pairs and quasar–star associations. Amongst the independently discovered quads is 2M1134–2103, for which we obtained spectroscopy for the first time, finding a redshift of 2.77 for the quasar. There is evidence for microlensing in at least one image. We perform detailed mass modeling of this system using archival imaging data, and find that the unusually large shear responsible for the diamond-like configuration can mainly be attributed to a faint companion $\sim 4''$ away, and to a galaxy group $\sim 30''$ away. We also set limits of $z \sim 0.5 - 1.5$ on the redshift of the lensing galaxy, based on its brightness, the image separation of the lensed images, and an analysis of the observed photometric flux ratios.

Key words: gravitational lensing: strong – quasars: individual: 2M1134–2103

1 INTRODUCTION

To date, nearly 40 quadruple¹ (quad) and nearly 120 double gravitationally lensed quasars are known. Their value as probes of cosmology and astrophysics has been explored observationally for the past four decades (e.g., see reviews by Claeskens & Surdej 2002; Treu & Marshall 2016), yet their number is still a limiting factor for many focused studies (e.g., Oguri et al. 2012; Schechter et al. 2014; Bonvin et al. 2017). We are currently in a post-Sloan Digital Sky Survey (SDSS; York et al. 2000) era when the large ongoing imaging surveys such as the Panoramic Survey Telescope and Rapid Response System (Pan-STARRS1, hereafter PS1; Chambers et al. 2016), the Dark Energy Survey (Flaugher et al. 2015) and the Hyper Suprime-Cam Subaru Strategic Program (Aihara et al. 2017) do not (yet) have a spectroscopic counterpart, making it difficult to identify

lensed quasars. As a result, contemporary dedicated searches for lensed quasars rely on selecting their candidates by applying machine learning techniques such as artificial neural networks (e.g., Agnello et al. 2015) or gaussian mixture models (e.g., Williams, Agnello, & Treu 2017) to multi-filter photometric catalogues in conjunction with pixel-by-pixel pattern recognition; by looking for flux and position offsets between these surveys and *Gaia* (e.g., Lindegren et al. 2016; Lemon et al. 2017; Agnello et al. 2017); and/or by complementing these with variability information (e.g., Berghea et al. 2017; Kostrzewa-Rutkowska et al. 2018).

Encouraged by the serendipitous discovery by Berghea et al. (2017) of the first quad from PS1, PSOJ0147, we have begun a systematic search for lensed quasars in this survey, by cross-correlating sources with the parent AGN catalogue of Secrest et al. (2015). As the first PS1 data was released in December 2016, mining it for lensed quasars has only recently begun (e.g., Ostrovski et al. 2018), making it likely that other lensed quasars, including bright, large separation quads, are yet to be found. Given the PS1 sky

* Subaru Fellow; e-mail: cerusu@naoj.org

¹ <http://masterlens.astro.utah.edu/>; also private communications

coverage and depth, [Oguri & Marshall \(2010\)](#) estimate that PS1 contains ~ 2000 lensed quasars, including 300 quads.

Recently, [Lucey et al. \(2017\)](#), hereafter L17) have announced the discovery of a new bright, large-separation quad, 2M1134–2103. This was a serendipitous discovery, as part of a search for extended 2MASS ([Skrutskie et al. 1997](#)) sources in the PS1 footprint, to include as targets for the Taipan Galaxy Survey ([da Cunha et al. 2017](#)). As part of our search, we have independently discovered this system. Here, we aim to present a more in-depth modeling of the archival imaging data, looking in particular to identify the cause for the unusually large shear inferred in L17. In addition, we present for the first time spectroscopic data for this system.

The structure of this paper is as follows: in Section 2 we describe our lensed quasar search technique and the current status, and present the new lens candidate sample. In Section 3 we describe our analysis of the archival imaging data of 2M1134–2103, and in Section 4 our newly acquired spectroscopic data. In Section 5 we present our mass modeling of 2M1134–2103, and provide plausible explanations for the unusually large shear. We conclude in Section 6. Where necessary, we use a flat cosmology with $\Omega_{\Lambda} = 0.74$ and $h = 0.72$.

2 A SEARCH FOR GRAVITATIONALLY LENSED QUASARS IN PS1

PS1 is a wide-field imaging system with a 1.8 m telescope and 7.7 deg^2 field of view, located on the summit of Haleakala in the Hawaiian island of Maui. The 1.4 Gpixel camera consists of 60 CCDs with pixel size of 0.256 arcsec ([Onaka & al. 2008](#); [Tonry & Onaka 2008](#)). The first PS1 data release includes both images and a photometry catalogue ([Chambers et al. 2016](#)). PS1 uses five SDSS-like filters (g_{P1} , r_{P1} , i_{P1} , z_{P1} , y_{P1}). The largest survey PS1 performs is the 3π survey, covering the entire sky north of -30 deg declination.

As we did for PSOJ0147, we start our search with the AGN candidates catalog of [Secrest et al. \(2015\)](#), based on two mid-infrared colors measured with the *Wide-field Infrared Survey Explorer* ([Wright et al. 2010](#)). We cross-correlate this catalog with the PS1 catalog using a $2''$ radius cone search and keep 48816 candidates which have at least two counterparts. Next we remove candidates within 15 degrees of the galactic plane. Finally, in order to eliminate globular clusters and similar crowded regions we impose the condition that there are no more than five counterparts within $20''$ radius. The final sample contains 8997 candidates.

We downloaded postage stamp color JPEG images of the candidates using the PS1 cutout service², which were then inspected visually by three of the authors (CTB, ES and GJT). Pairs with separation \lesssim a few arcsec between components (consistent with strong lensing by galaxies) and similar colors, triplets with a redder inner component, as well as quads with configurations consistent with canonical lensing configurations were kept. Finally, the other three authors (CER, CDF and AM) graded the remaining sample of 73

candidates judging again by visual appearance, the presence of extended emission or of nearby stars of similar colors (indicating likely stellar contaminants). As is customary in the lens search community, we use the following grading system: 0: unlikely to be a lens; 1: possibly a lens candidate (satisfies only some criteria to be a lens); 2: probably a lens candidate (satisfies most criteria to be a lens); 3: almost certainly a lens (there is almost no doubt that this is a lens). To check for possible emission from the lensing galaxy between bright point sources, we fitted and subtracted the point sources in each post-stamp image (typically in i -band, unless the seeing was better in other bands) using *hostlens* ([Rusu et al. 2016](#)). *Hostlens* models an arbitrary number of point-like and extended sources using a common point-spread function (PSF), fitted to the data as a sum of two concentric Moffat ([Moffat 1969](#)) profiles. Excluding outstanding red star interlopers, we found such emissions in 10 candidates, although the data are of insufficient quality to resolve them.³

We discover a total of 5 known quads: PSOJ0147, 2M1134-2103, HE 0435-1223, ([Wisotzki et al. 2002](#)), SDSS J1433+6007 ([Agnello et al. 2018](#)) and another one in Lemon et al. in prep (private communications), as well as one known double, SDSS J1206+4332 ([Oguri et al. 2005](#)). We note that other known quads with bright lenses, such as 2M1310-1714 (L17), are not included in our sample because the lens light contaminates the infrared colors that the [Secrest et al. \(2015\)](#) AGN catalog is based on. [Secrest et al. \(2015\)](#) note that the chance of misclassifying stars in the AGN catalogue is $\leq 0.041\%$, so we expect that the main contaminants to our list of candidates, after visual examination, will be quasar + star pairs as well as quasar pairs, as either physically associated binary quasars or projected chance alignments. We give positive grades to quasar pairs without signs of additional emission for two reasons: first, the lensing galaxy may be faint, at high redshift, or difficult to separate from the residuals of the *hostlens* PSF subtraction. Indeed, this is the case in the PS1 data of 2M1134–2103 (Section 3). Second, because rather than focusing on producing the purest lensed quasar sample, we prefer to include in our sample binary quasars, which may be of interest to the AGN community.

We present our sample of gravitationally lensed quasar candidates that survived visual examination in Table 1, together with our comments. In the following sections, we focus on modeling imaging and spectroscopic data of 2M1134–2103.

3 2M1134–2103: IMAGING DATA REDUCTION AND MODELING

2M1134–2103 consists of four point-like lensed quasar images and a lensing galaxy (see Fig. 1). The lensing galaxy 2M1134–2103 can be convincingly identified in the near-infrared imaging (particularly K_s -band) from the VISTA Hemisphere Survey (hereafter VHS; [McMahon et al. 2013](#), see also Fig. 1). While the relative astrometry of the quasar images, measured from VLT-ATLAS ([Shanks et al. 2015](#)), is

² http://hla.stsci.edu/fitscutcgi_interface.html

³ For example, in the known lens SDSS J1206+4332 the lensing galaxy appears well-fitted with a point source in the PS1 data.

Table 1. Sample of gravitationally lensed quasar candidates identified systematically from PS1

Designation	α	δ	#Comp	i	Sep. ["]	Rank	Notes
PS1 J011133+373824	17.89103	+37.64015	3	15.90	2.5	C	similar color pair + faint star
PS1 J011401–054257	18.50594	–5.71607	2	16.21	1.4	C	similar color pair
PS1 J012255+783854	20.73332	+78.64854	2	18.43	2.0	C	similar color pair
PS1 J012634–291540	21.64250	–29.26130	3	14.93 ¹	1.5	C	similar color pair + faint red object
PS1 J014710+463043	26.79244	+46.51217	4	15.58	3.8	A	four point sources in a quad cusp configuration; known quad PS0J0147 (Berghea et al. 2017; Rubin et al. 2017; Lee 2017, 2018)
PS1 J021412+461825	33.55000	+46.30722	2	16.15	2.1	C	similar color pair with galaxy in between (Keck NIRC2 +AO imaging); not a lens (Keck ESI spectroscopy)
PS1 J022346–104635	35.94391	–10.77657	3	15.58 ¹	1.0	C	similar color pair + red star
PS1 J025456–002525	43.73594	–0.42364	2	15.08 ¹	2.0	C	similar color pair
PS1 J025901–262220	44.75756	–26.37235	2	15.57	1.0	C	similar color pair
PS1 J035315+521300	58.31658	+52.21692	2	14.63 ¹	0.8	C	similar color pair
PS1 J035450–081843	58.71128	–8.31217	3	14.98	4.1	C	similar color pair + faint blue object
PS1 J035722–104510	59.34347	–10.75281	3	15.56	4.7	C	similar color pair + yellow inner component
PS1 J040711–022338	61.79856	–2.39407	5	16.28	7.2	B	bright blue object surrounded by four red objects ^a
PS1 J043814–121714	69.56160	–12.28748	5	17.33 ¹	2.6	A	four objects surrounding inner component; known quad HE 0435–1223 (Wisotzki et al. 2002)
PS1 J050223+095136	75.59649	+9.86002	3	18.79	3.3	C	similar color pair near large galaxy
PS1 J050707–200854	76.77962	–20.14838	3	16.05	2.1	C	similar color pair + faint red object
PS1 J053019–184826	82.58025	–18.80740	2	13.89	1.8	C	similar color pair
PS1 J054131–240740	85.37927	–24.12785	3	15.37	6.1	B	similar color pair + red inner component
PS1 J054630–255209	86.62695	–25.86920	3	16.33	2.9	C	similar color pair + faint red object
PS1 J083733+574803	129.38797	+57.80092	2	15.32 ¹	1.6	C	similar color pair
PS1 J084440+334909	131.16940	+33.81917	2	18.28	2.9	C	similar color pair
PS1 J085328–032513	133.36990	–3.42050	3	18.71	4.6	C	extended emission between blue point sources
PS1 J090145+851434	135.43942	+85.24284	2	15.53	1.8	C	similar color pair
PS1 J091430–023746	138.62720	–2.62961	2	16.01	2.4	C	similar color pair
PS1 J091723–054200	139.34830	–5.70007	2	18.80	2.5	C	similar color pair
PS1 J092718+211357	141.82660	+21.23261	2	17.51	2.3	C	similar color pair
PS1 J094020+523714	145.08424	+52.62060	2	15.58	0.8	C	similar color pair
PS1 J102356+705337	155.98431	+70.89381	3	16.41	2.2	B	similar color pair + red inner component; not a lens (Keck ESI spectroscopy)
PS1 J104703–241459	161.76560	–24.24980	3	16.96	2.8	B	similar color pair + red inner component
PS1 J112456–230507	171.23370	–23.08550	2	18.94	1.9	C	similar color pair
PS1 J113145–115102	172.94160	–11.85056	3	15.82	3.6	C	similar color pair + faint red object
PS1 J113440–210323	173.66910	–21.05643	4	16.81	3.7	A	four point sources in a diamond configuration; known quad 2M1134–2103 (L17)
PS1 J113525–250551	173.85610	–25.09777	3	12.79	5.4	B	similar color pair + red inner component
PS1 J115537–232128	178.90809	–23.35789	3	17.45	2.3	C	similar color pair + yellow star
PS1 J120629+433220	181.62360	+43.53906	3	18.52	3.0	B	similar color pair + red inner component; known double J1206 + 4332 (Oguri et al. 2005)
PS1 J123558–023503	188.99400	–2.58423	2	17.79	3.0	C	similar color pair
PS1 J133616–142737	204.06690	–14.46050	2	17.72	2.8	C	similar color pair + red inner component
PS1 J134602+035537	206.50921	+3.92720	3	16.10	2.6	C	similar color pair + red star
PS1 J143322+600713	218.34500	+60.12038	5	19.49	3.7	A	four blue objects surrounding inner component; known quad SDSS J1433+6007 (Agnello et al. 2018)
PS1 J151752+135619	229.46772	+13.93869	2	15.73 ¹	1.0	B	similar color pair
PS1 J152304+351012	230.76689	+35.17015	3	16.01	3.3	C	similar color pair + red object
PS1 J154232+325830	235.63420	+32.97501	2	19.18	3.2	C	similar color pair
PS1 J160020+102430	240.08597	+10.40845	3	17.43	4.2	C	similar color pair + yellow star
PS1 J161405+035305	243.52252	+3.88496	3	14.96	2.9	C	similar color pair + red star
PS1 J161721–230546	244.34010	–23.09620	2	18.81	1.9	C	similar color pair
PS1 J164012+194004	250.05196	+19.66780	3	15.17	2.6	C	similar color pair + faint red object
PS1 J170817+325311	257.07250	+32.88643	2	18.39	2.1	C	similar color pair
PS1 J171101+292950	257.75710	+29.49749	2	17.92	2.2	C	similar color pair
PS1 J180257+244144	270.73760	+24.69567	3	18.50	4.3	B	similar color pair + extended yellow component
PS1 J192651+224513	291.71390	+22.75368	2	13.87 ¹	1.6	C	similar color pair
PS1 J205143–111444	312.93090	–11.24560	4	18.95	3.3	B	four blue objects in a cusp quad configuration ^b
PS1 J223445–144920	338.68750	–14.82240	2	15.88	2.2	C	similar color pair
PS1 J234155+132901	355.48060	+13.48380	2	18.82	3.2	C	similar color pair

Here α and δ are the International Celestial Reference System (ICRS) right ascension and declination of the candidates. In “#Comp”, which refers to the number of components, we count any object within a radius similar to the separation between the main point sources used to identify the candidate systems, such as possible line of sight contaminants. The measured separation (“Sep.”, in arcseconds) is that between the lens candidate point sources or, in case of a quad, the maximum separation between any of the point sources. The magnitude is given in i -band in the AB system for the brightest resolved component. We quote the *i*MeanPSFMag measurements from the catalogue at <http://archive.stsci.edu/panstarrs/search.php>; for close separation unresolved systems marked with ¹ we quote the aperture magnitude *i*MeanApMag. We list in this table alphabetic ranking for all systems with an average grade of 1 and above, based on three human graders, as detailed in Section 2, with the exception of one unpublished quad (Lemon et al., in prep). We follow the following convention for the alphabetic ranking: A: average grade > 2.5; B: average grade > 1.5; C: average grade \geq 1.

^a PS1 imaging suggests a quasar lensing a high- z galaxy, but modeling the observed configuration with *glafic* results in a large χ^2 value.

^b *Glafic* modeling of the observed configuration results in a perfect fit, but the model is underconstrained.

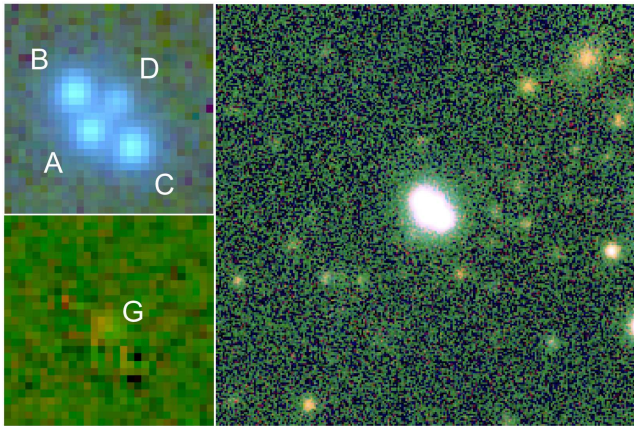


Figure 1. *Upper left:* Color composite (VHS- $YJKs$) of 2M1134–2103 showing the four lensed quasar images (A, B, C and D). Image is $10''$ on the side. *Lower left:* The same color composite, after subtracting the four quasar images with `hostlens`, shows the presence of a lensing galaxy G. *Right:* Color composite (riz) using PS1 data shows the immediate environment of the lens system, which is located at the center. Image is $60''$ on the side. All images are oriented such that North is up and East is to the left.

reported in L17, the VLT-ATLAS data is not publicly accessible. Furthermore, the VLT-ATLAS data have better seeing ($0.72''$) but the PS1 data are deeper. Therefore, we make use of archival PS1 data in our analysis. The processing of the archival PS1 data (Flewelling et al. 2016) is described in (Magnier et al. 2016a), and includes removal of the instrumental signature, image coaddition, as well as photometric and astrometric calibration (Magnier et al. 2016b). Here, we model the PS1 $grizy$ and VHS $YJKs$ images independently of L17.

For our detailed modeling of 2M1134–2103 we downloaded from the PS1 and VHS archives $180'' \times 180''$ cutouts around the system in all available filters, large enough to contain stars to model the PSF and to improve the image orientation. We subtracted the sky background from the VHS images using `SExtractor` (Bertin & Arnouts 1996), and re-sampled all images with `Swarp` (Bertin et al. 2002) to a common orientation. We measured final pixel scales with `Scamp` (Bertin 2006).

We find that modeling the quasar images using nearby stars as PSFs results in significant residuals, which could affect the image flux measurements and the characterization of the lensing galaxy. We therefore use `hostlens` to improve the fitting in all bands, using an analytical PSF fitted to the data. To remove residuals still remaining at the centers of the three bright quasar images in the $rizYJKs$ bands, we use the PSF reconstruction technique described in Chen et al. (2016), with the best-fit analytical PSF as a starting point. This technique reconstructs the PSF iteratively, on a grid of pixels, under the assumption that the PSF does not vary across the quasar images. The remaining residuals at the location of the quasar images are small, as can be seen in Fig. 2.

In the PS1 data we do not detect any sign of the lensing galaxy, which however stands out in the VHS J and Ks images. We model its light profile in these bands simultaneously with the quasar images, using a de Vaucouleurs

(de Vaucouleurs 1948) profile commonly used for early-type lensing galaxies. A circular profile fits the emission from the lensing galaxy well, without leaving noticeable residuals. Using a Markov Chain Monte Carlo (MCMC) approach, we find that the lensing galaxy flux is highly degenerate with the effective radius of the de Vaucouleurs profile, and is therefore unreliable.

In order to perform gravitational lens modeling of 2M1134–2103 we need to estimate reliable relative astrometry for the quasar images and the lensing galaxy. For the three brightest quasar images we take the mean and scatter between the measured relative astrometry in different filters (excluding g -band, where the seeing is significantly larger, see Table 2), whereas for the lensing galaxy and the faint counter-image D, we only use the J and Ks filters. Indeed, the separation between the brighter images (A, B and C) and the fainter counter-image D decreases slightly with increasing wavelength in the PS1 images, because of the progressively increasing flux contribution from the red lensing galaxy. We report our measured astrometry and photometry in Table 2. Our astrometry is consistent with the one presented in L17 within our 2σ uncertainties.

4 2M1134–2103: KECK SPECTROSCOPY

The 2M1134–2103 lens system was observed with the Echellette Spectrograph and Imager (ESI; Sheinin et al. 2002) on the night of 2017 Nov 18 UT (program number 2017B_U110). The observations utilized a slit with a width of $1''$ and the cross-dispersed echellette mode of the spectrograph, which provides a constant dispersion of roughly $11.5 \text{ km sec}^{-1} \text{ pix}^{-1}$ over a wavelength range of approximately 3900 to 11000 Å. Here, we follow the nomenclature of L17. Two slit position angles were used, one oriented at $+46.7^\circ$ (N through E) in order to go across lensed images B and C (henceforth the “BC slit”) and one oriented at -42.3° to cover images A and D (the “AD slit”). We obtained three 600 s exposures through the BC slit and four 600 s exposures through the AD slit.

We calibrated the data using a custom pipeline written in Python. The pipeline does a flat-field correction, rectifies the two dimensional spectra, does the wavelength calibration using both arc lamp and night sky emission lines, and subtracts the sky emission. The calibrated data for both slits are shown in Fig. 3. In the AD slit, the two-dimensional spectra show one bright trace that is heavily blended with a much fainter trace, while the BC slit shows three clearly separated traces. We identify the three traces in the BC slit with components B, A+D+G, and C in the imaging data. Based on the imaging, we expect that the emission from image A completely dominates the central trace.

We extracted one-dimensional spectra from the exposures on both slits using a second Python pipeline that extracts the spectra from each spectral order, applies a response correction based on observations of a spectrophotometric standard, in this case Feige 110, and finally combines the data from each of the 10 spectral orders into one final spectrum. For the AD slit, we only extracted one aperture that we identify with a blend of A, D, and G, while for the BC slit we extracted separate apertures corresponding to B, A+D+G, and C. Note that the AD slit may very well con-

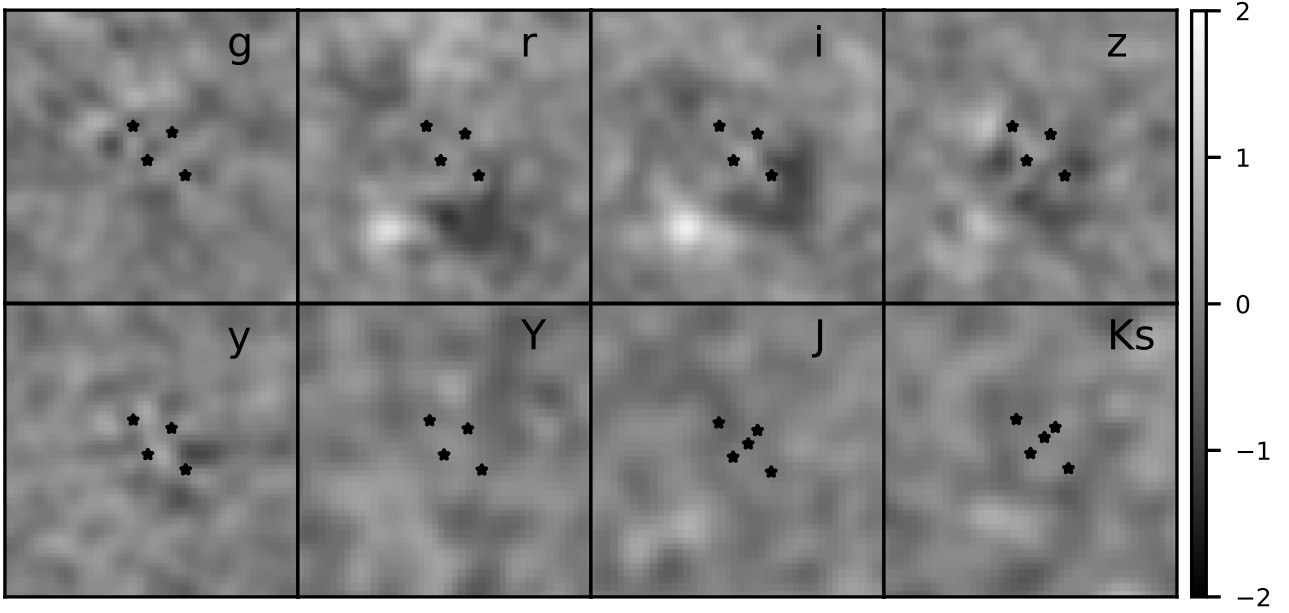


Figure 2. Residuals after morphological modeling of imaging data with *hostlens*. The size of the cutouts is $15'' \times 15''$. The images were divided by the associated noise maps, then smoothed with a 3-pixel Gaussian, to enhance structure. The positions of the components that were modeled in each band (A, B, C, D, as well as G in *JKs*) are marked with star symbols. Object GX to the south-east of the lens, conspicuous in the *r* and *i* bands, is left unmodeled (see Section 5) .

Table 2. Relative astrometry and absolute photometry of 2M1134–2103

Filter (lim. mag)	A	B	C	D	G	GX	Seeing ["]
all (x-axis)	0.000 ± 0.000	-0.733 ± 0.005	1.944 ± 0.006	1.262 ± 0.014	0.74 ± 0.04	-2.50 ± 0.05	
all (y-axis)	0.000 ± 0.000	1.757 ± 0.006	-0.776 ± 0.006	1.350 ± 0.020	0.75 ± 0.10	-3.32 ± 0.05	
<i>g</i> (24.2)	17.08 ± 0.005	17.37 ± 0.005	17.26 ± 0.005	18.90 ± 0.014	–	–	1.70
<i>r</i> (24.5)	16.85 ± 0.005	17.06 ± 0.005	17.00 ± 0.005	18.67 ± 0.005	–	$[23.37 \pm 0.10]$	1.20
<i>i</i> (24.5)	16.81 ± 0.005	16.88 ± 0.005	16.83 ± 0.005	18.46 ± 0.005	–	$[21.75 \pm 0.08]$	1.20
<i>z</i> (23.6)	16.87 ± 0.005	16.90 ± 0.005	16.87 ± 0.005	18.49 ± 0.006	–	–	1.10
<i>y</i> (22.6)	16.79 ± 0.04	16.72 ± 0.03	16.70 ± 0.03	18.29 ± 0.04	–	–	1.00
<i>Y</i> (22.2)	16.08 ± 0.008	15.98 ± 0.007	16.02 ± 0.007	17.57 ± 0.016	–	–	0.85
<i>J</i> (21.4)	15.92 ± 0.005	15.81 ± 0.005	15.83 ± 0.005	17.35 ± 0.012	$[19.05 \pm 0.12]$	–	0.85
<i>Ks</i> (20.1)	15.34 ± 0.006	15.13 ± 0.006	15.19 ± 0.009	16.81 ± 0.027	$[17.33 \pm 0.09]$	–	0.85

Relative astrometry is determined by using information from multiple filters (See Section 3). The units are arcseconds and the sign convention is positive from E to W (x-axis) and from S to N (y-axis). The ICRS position of image A in the PS1 catalogue is (J2000.0) 11:34:40.588 –21:03:23.06. Magnitudes are in the AB (*grizy*) and Vega (*YJKs*) systems, and are corrected for Galactic extinction following Schlafly & Finkbeiner (2011). The 1σ limiting magnitudes are computed in $2''$ -radius blank sky apertures around the system. The errors on magnitudes are those from MCMC, with the minimum uncertainty boosted to 0.005 mag, and do not include zeropoint or PSF uncertainties. The magnitudes of G and GX (see Section 5) should be considered unreliable, as in order for the fit to converge, the effective radius was fixed to < 1 pixel.

tain significant scattered light from images B and C. The extracted spectra are shown in Fig. 4 and all show clear broad emission lines that, furthermore, are indicative of quasars at a redshift of $z_{\text{src}} \sim 2.77$. Thus, the ESI spectra are fully consistent with the interpretation of 2M1134–2103 as a quad lensed quasar. An exact value of the source redshift is difficult to obtain due to the fact that the peaks of the lines used for redshift determination are affected by absorption systems (Fig. 4; also e.g., Lee 2018). The measured redshift is smaller than the $z \sim 3.5$ estimate in L17, based on PS1 colors.

In addition to the broad emission lines, all of the spectra show a number of absorption lines. In the range 5000–7500Å, these correspond to absorption features of Fe and Mg, and are consistent with two separate absorption systems at $z_{\text{abs},1} = 1.554$ and $z_{\text{abs},2} = 1.481$. The first system has stronger lines in the A+D+G and B spectra, while the second is stronger in the image C spectrum. Although it is possible that these systems may be associated with the primary lensing galaxy, the narrowness of the lines makes this interpretation unlikely. A much stronger indication of the lensing galaxy would be the detection of stellar absorption

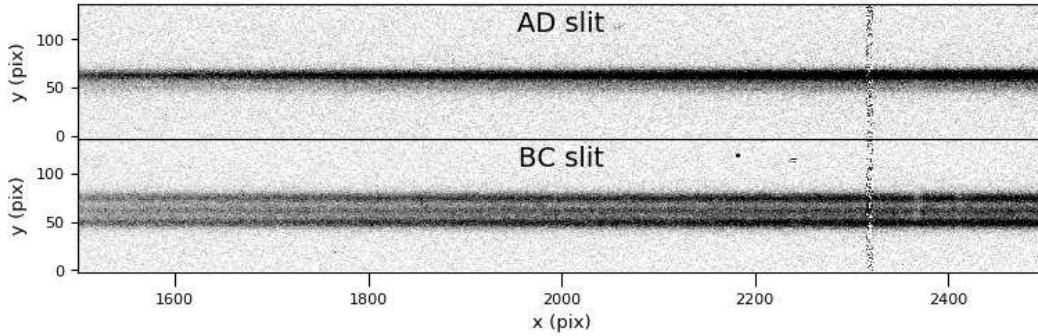


Figure 3. Examples of the calibrated and sky-subtracted spectra obtained with Keck/ESI of 2M1134–2103. Data are from the AD slit (top) and the BC slit (bottom), with spectra showing a portion of the fifth of ten spectral orders recorded by the spectrograph.

lines, such as the CaII H and K lines, with widths consistent with the velocity dispersions of $>100 \text{ km s}^{-1}$ expected for a massive lensing galaxy. If these corresponded to the redshifts of the absorption features mentioned above, they would be observed at wavelengths longer than the ones plotted in Fig. 4, where we have extracted robust spectra.

5 2M1134–2103: GRAVITATIONAL LENS MODELING

We perform gravitational lens mass modeling of 2M1134–2103 with *glafic* (Oguri 2010), using the observed relative positions of the quasar images and the lensing galaxy as constraints. We do not impose constraints based on the flux ratios, as these might be affected by microlensing, extinction, and intrinsic variability (e.g., Yonehara, Hirashita, & Richter 2008). However, we analyze the observed flux ratios under the assumptions that they are dominated by extinction, in Section 5.1.

We start with the same mass model used in L17, a singular isothermal sphere with external shear (SIS+ γ). This model has $\chi^2/\text{d.o.f.} = 7.5/3$ (where d.o.f. stands for degrees of freedom), most of which is due to the difference between the measured and predicted position of image D relative to the lens G. We recover the results of L17, in particular that an unusually large shear of ~ 0.34 at 44 deg W of N is required to fit this system.

Secondly, we fit a model which allows for mass ellipticity, SIE+ γ . Indeed, quads have enough constraints to disentangle internal and external sources of shear, and our fit shows a dramatic improvement to $\chi^2/\text{d.o.f.} = 0.1/1$. This model requires a shear of ~ 0.39 , slightly larger than before, and a mass axis ratio of $0.80^{+0.10}_{-0.18}$, with the long axis at 37^{+5}_{-13} deg E of N, almost perpendicular to that of the shear. While our imaging data does not have sufficient resolution to fit an elliptical light profile to the lensing galaxy, studies of quads show that the mass and light profiles of lensing galaxies are typically aligned (e.g., Keeton, Kochanek, & Falco 1998; Sluse et al. 2012).

As both the SIS+ γ and SIE+ γ models are consistent in their requirement of large external shear, we look for potential sources of shear from the surrounding environment. In Fig. 1 we display a $60'' \times 60''$ color composite image around 2M1134–2103, which clearly shows a group of red galaxies in

the upper right corner, the brightest of which is a $i = 19.32$ galaxy located at $\alpha = 173.6620$, $\delta = -21.0502$, $30''$ from the quad, in the direction of 45 deg W of N. The PS1 and VHS colors of this galaxy imply a photometric redshift of 0.70 ± 0.09 , estimated with BPZ (Benítez 2000). The existence of the galaxy group at this location implies that it is responsible for part of the measured shear. However this is unlikely to be the complete picture, as an SIS profile at the location of this galaxy would require a velocity dispersion of $\gtrsim 1100 \text{ km/s}$ to produce the measured shear, depending on the redshift of the lensing galaxy in 2M1134–2103.

Fig. 2 reveals another clue, closer to 2M1134–2103. After subtracting the quasar images, an additional component is detected in filters r and i , $4.16''$ from image A, also in the direction of the shear, towards south-east. It is unclear whether this new component, which we name GX, is a galaxy or a star, as it is too faint ($i \sim 21.75$) to constrain its morphology. Under the assumption that it is a galaxy, its colors suggest a redshift lower than the one of the lensing galaxy, which is only detected in the near-infrared VHS filters. We incorporate GX into a third lensing model, in order to estimate its effect on the external shear. As we do not know the redshifts for either G or GX, we consider the simplest case in which G and GX are modeled as SIS of equal strength, at the same redshift. This model is expected to be an upper limit to the contribution of GX to the lensing configuration, as GX is likely a lower redshift, low mass galaxy. We obtain a good fit with $\chi^2/\text{d.o.f.} = 2.3/3$, and a residual external shear of ~ 0.19 , oriented as before. In this model, the two lenses are located ~ 4 Einstein radii apart, in units of the Einstein radius of G. Our model shows that GX can explain a significant fraction of the shear we measured in our initial SIS+ γ model. We expect that in reality most of the measured shear is an interplay between the effects of GX and the nearby group.

In the analysis above we did not assume particular values of source and lens redshifts, except when we estimated the velocity dispersion of the galaxy group at $z \sim 0.7$. The flux ratios are also insensitive to the choice of redshifts, however the estimated time delays depend on them. To estimate the time delays, which are of interest to cosmography studies (e.g., Bonvin et al. 2017), we use the source quasar redshift $z_s = 2.77$ measured from spectroscopy, and the lens redshift limits we infer below in Section 5.1, $z_l \sim 0.45 - 1.5$. For $z_l \sim 0.45$ and the SIS+ γ model, the estimated time delays

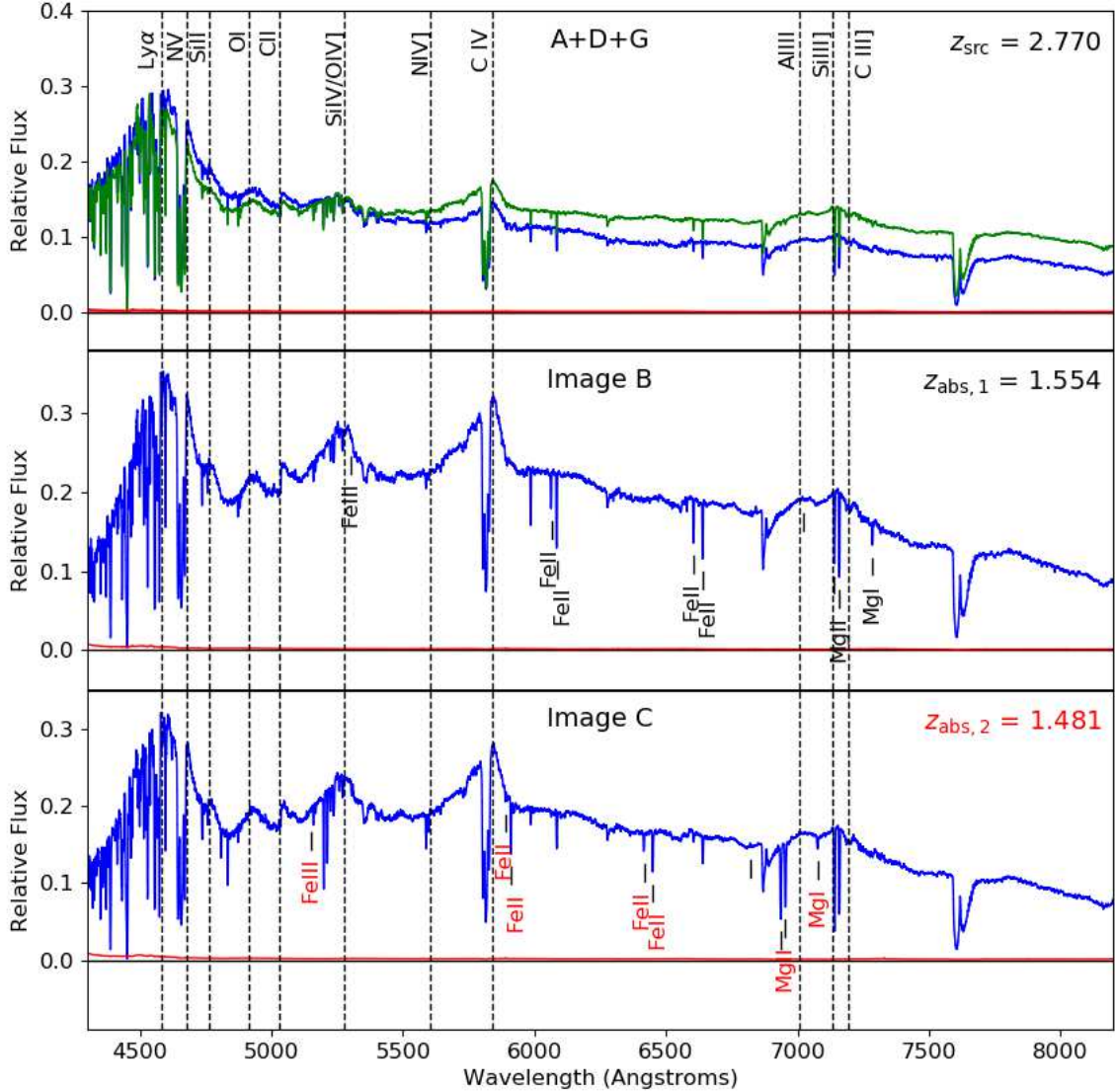


Figure 4. ESI spectra of 2M1134–2103. Combined light from lensed images A and D, plus any emission from the lensing galaxy is visible in the spectrum extracted from the AD slit (green) as well as that from the BC slit (blue) in the top panel. Spectra of images B (middle) and C (bottom) are extracted from the BC slit. The rms noise of each spectrum is plotted in red. Identified emission and absorption systems are labelled (see further explanation in Section 4). The wide absorption doublet at ~ 7650 Å is telluric. The spectra were smoothed using a 3-pixel boxcar with inverse-variance weighting.

are $\Delta_{CB} \sim 7$ days, $\Delta_{CA} \sim 30$ days and $\Delta_{CD} \sim 55$ days. The order of the image time arrival is the same in all three models, with image C leading. We summarize the main parameters of the mass models we employed in Table 3, along with the corresponding time delays.

5.1 Flux ratio analysis and the lens redshift

We show the measured image flux ratios in Fig. 5, based on Table 2. Most of the six ratios show a clear dependence on wavelength. Interpreted as due to extinction, these ratios imply that A is the least reddened image, in agreement with image D being closest to the lensing galaxy, and the major axis of the lensing galaxy being oriented towards B and C, according to the SIE+ γ model. We also show in Fig. 5

Table 3. Summary of the best-fit parameter values of the lensing mass models, and the predicted time delays

Model	z	σ [km/s]	e	θ_e	γ	θ_γ	ΔCA	ΔCB	ΔCD
SIS+ γ	0.45	243.0	—	—	0.34	43.6	30.5	6.8	54.8
SIS+ γ	1.50	384.1	—	—	0.34	43.6	196.6	43.9	353.1
SIE+ γ	0.45	242.1	0.33	−39.9	0.39	45.2	24.7	6.3	43.6
SIE+ γ	1.50	382.6	0.33	−39.9	0.39	45.2	159.0	40.3	281.0
2SIS+ γ	0.45	233.3	—	—	0.19	45.8	33.9	7.5	44.3
2SIS+ γ	1.50	363.4	—	—	0.19	45.8	225.9	49.3	263.4

Here z is the lens redshift, σ is the lens velocity dispersion, e and γ are the lens ellipticity and shear, respectively, and θ_e and θ_γ are their orientations (W of N). The time delays (last column) are in units of days.

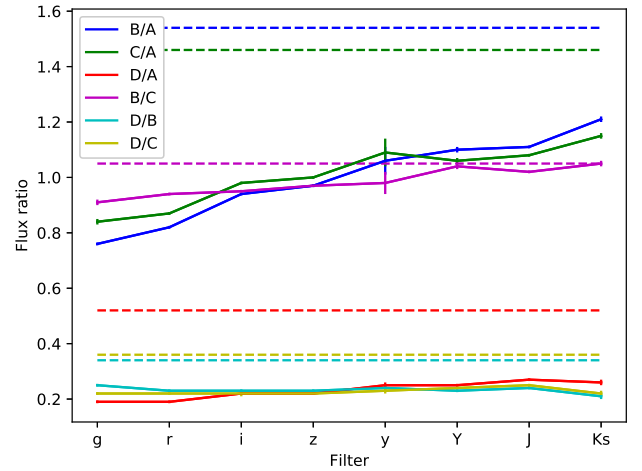
the predicted flux ratios given by the SIS+ γ model. All predicted ratios are above the measured ones, again consistent with extinction. The predicted SIE+ γ fluxes are very similar, within $\sim 10\%$, but the G+GX+ γ model predicts a demagnified image A, about as bright as D. All models predict image B to be the brightest, as observed in the VHS data. The predicted B/C is invariant across all three models, as the shear is almost perpendicular to the direction of these two images. In fact, this ratio is the only one which matches the observations, in the reddest filter.

Flux ratios of quasar images have been used in the past to study the extinction properties of lensing galaxies (e.g., Falco et al. 1999) as well as to infer lens redshifts (e.g., Jean & Surdej 1998). Here, we use them to infer the lens redshift z_l as well as the de-reddened flux ratios (relative magnifications) M_i , where i refers to each of the six image pairs, independent of the chosen mass model. Following Falco et al. (1999), we optimize these parameters as well as the differential extinctions E_i and the shape of the extinction curve R by minimizing

$$\chi^2 = \sum_{j=1}^{N_\lambda} \sum_{i=1}^{N_{\text{imag}}} \frac{\left[m_i^r(\lambda_j) - m_i^b(\lambda_j) - 2.5 \log M_i - E_i R \left(\frac{\lambda_j}{1+z_l} \right) \right]^2}{\sigma_{ij}^{b,2} + \sigma_{ij}^{r,2}} \quad (1)$$

where j is the filter index, superscripts b and r refer to the blue and red images in each pair, respectively, and σ_{ij} is the magnitude measurement uncertainty. We use the central wavelength of each filter, and the Cardelli, Clayton, & Mathis (1989) extinction function implemented in the code `extinction`⁴. We perform the minimization using the Nelder-Mead (Nelder & Mead 1965) method implemented in `Scipy` (Oliphant 2007), starting from random positions in the parameter space and further exploring around the solution with `emcee` (Foreman-Mackey et al. 2013), to ensure that we have found the global solution.

We find the best-fit solution ($\chi^2/\text{d.o.f.} = 213.4/37$) with $z_l \sim 0.45$, $R \sim 2.5$ slightly smaller than the Galactic extinction curve with $R_V = 3.1$, small $E_i \lesssim 0.1$ consistent with the results in Falco et al. (1999), and flux ratios B/A = 1.28, C/A = 1.20, D/A = 0.30. These parameter values are robust if we remove from the fit all image pairs containing D (new fit $\chi^2/\text{d.o.f.} = 145.8/17$), in case our decomposition

**Figure 5.** Measured and model-predicted flux ratios of the four quasar images. Solid lines connect observed flux ratios in all available filters, and dashed lines of corresponding colors mark the flux ratios predicted by the SIS+ γ lens mass model.

of G and D is problematic due to the low image resolution. They are also robust to the choice of the extinction function. Except for B/C, which matches the prediction of the mass models, the flux ratios are smaller than predicted. The quality of the fits is statistically rather poor, although such large χ^2 values are found by e.g., Falco et al. (1999) in other lensing systems as well. In our analysis, we have ignored any contribution from microlensing and quasar intrinsic variability, which can also affect flux ratios chromatically (e.g., Yonehara, Hirashita, & Richter 2008).

We can look for signs of microlensing by plotting the quasar image spectral ratios. While the overall shape of these ratios is sensitive to observational effects such as sub-optimal slit placement and differential refraction, these (as well as differential extinction) should affect both continua and emission lines equally. On the other hand, microlensing is dependent on the size of the source, such that the continuum emission, which originates from a more compact region than the broad emission lines, should be preferentially microlensed. Fig. 6 clearly shows that, when dividing the fluxes of B and C to those of A_{BC} (i.e. the A+D+G signal, dominated by A, and extracted from the BC slit) and of A_{AD}, there is a large jump in the flux ratios at the locations of the SiV/OIV] ($\sim 5270\text{\AA}$) and CIV ($\sim 5800\text{\AA}$) broad line regions, compared to the surrounding continuum. On the other hand, B/C is relatively flat over the entire plotted

⁴ <http://extinction.readthedocs.io/en/latest/>

range, which means that microlensing affects image A+D (the saddle points of the time arrival surface) but not B and C. A direct comparison of the photometric flux ratios in Fig. 5 with the spectroscopic ratios in Fig. 6 is not possible due to the fact that the spectra are affected by slit losses. Indeed, this can be seen from the monotonic variation in A_{AD}/A_{BC} , which we attribute to the fact that ESI does not use an atmospheric dispersion corrector, thus resulting in flux losses from differential refraction, particularly between the orthogonally placed AD and BC slits. Also, the datasets are not concurrent, and are therefore prone to time-varying microlensing and intrinsic variability effects.

As discussed above, microlensing in particular may affect the inferred lens redshift. We note that due to the low image resolution, proximity to image D, and morphological compactness which may affect the extracted photometry, we could not obtain a robust photometric redshift for this galaxy. Looser but more robust redshift constraints can be set by using the observed image separation and the estimated magnitude of the lens in the filter in which it is brightest. On the one hand, the image separation gives the lens velocity dispersion as a function of redshift; on the other, assuming an early-type spectral template, the measured magnitude can be converted into a rest-frame absolute magnitude as a function of redshift⁵, and then into a velocity dispersion (Faber & Jackson 1976). We find a lower limit of $z_l \sim 0.5$, below which the two velocity dispersion estimates disagree, and an upper limit of $z_l \sim 1.5$, above which the lens velocity dispersion is ~ 400 km/s, a value above which the galaxy velocity dispersion function is vanishingly small (Sheth et al. 2003). The lower limit is close to the value inferred from our flux ratio analysis, and the upper one is consistent with the redshift of the narrow absorption systems identified in Section 4; it is also above the L17 estimate of $z_l \sim 1$.

6 CONCLUSIONS AND FUTURE WORK

We have carried out a systematic search for gravitationally lensed quasars in PS1, based on visual examination of cutouts around the AGN source catalogue of Secrest et al. (2015). We present our sample of 54 promising candidates in Table 1 in order to enable follow-up observations by the interested community. We expect that the main source of contaminants are quasar + star pairs, as well as quasar pairs. As part of our search, we have independently discovered five known quads, including 2M1134–2103. We present, for the first time, spectroscopy of this system, confirming it as a lensed quasar with source redshift $z \sim 2.77$. We identify absorption systems at $z \sim 1.5$, in three of the resolved quasar images, but we find these to be too narrow to attribute to the lensing galaxy. The image flux ratios show a monotonic dependence on wavelength, which we use to obtain a rough estimate of the lens redshift, under the assumption that the dependence is caused by extinction. The spectral flux ratios show evidence of microlensing in the combined emission from images A and D.

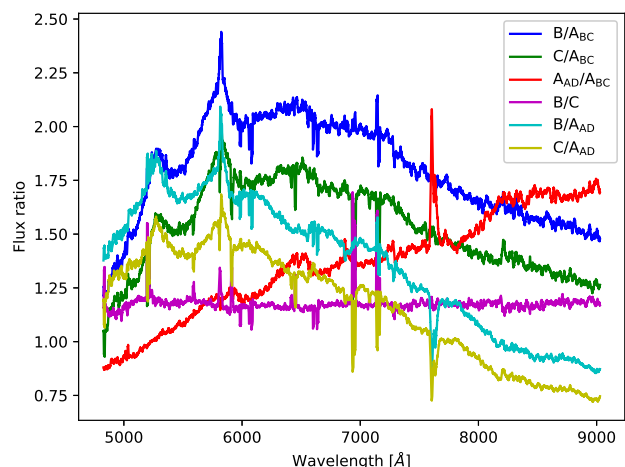


Figure 6. Measured spectral flux ratios in the region 4830 Å–9030 Å, where the measurements are robust. The colors correspond to those in Fig. 5, except that some flux ratios have been inverted and photometric ratios involving image D have been replaced with spectroscopic ratios of A_{AD} . The spikes correspond to the intrinsic or atmospheric absorption lines in the original spectra.

Our mass modeling confirms that 2M1134–2103 is affected by large shear, for which we identify two potential sources: a group of galaxies at $z \sim 0.7$, $30''$ from the lens, and another faint companion $\sim 4''$ away. Future multi-object spectroscopy is required to determine whether these are part of a larger cluster, or physically associated with the lens. The large image separation, brightness and estimated time delays ranging from several days to several months, depending on the lens redshift, make this a valuable system to use for cosmography (e.g., Bonvin et al. 2017), provided that the environment can be characterized with future, deep imaging and spectroscopy (e.g., Sluse et al. 2017; Rusu et al. 2017; Wilson et al. 2016). High resolution *Hubble Space Telescope* or adaptive optics imaging is necessary to constrain the morphology of the lensing galaxy, and to further constrain the mass models using the expected extended emission from the underlying host galaxy (e.g., Chen et al. 2016; Wong et al. 2017).

ACKNOWLEDGEMENTS

The authors wish to thank Paul L. Schechter for his “match-making” which has made this paper possible, and Chih-Fan Chen for granting access to his iterative PSF reconstruction code. This research made use of *Astropy*, a community-developed core Python package for Astronomy (Astropy Collaboration et al. 2013). Plots were produced with *Matplotlib* (Hunter 2007). This work was supported by World Premier International Research Center Initiative (WPI Initiative), MEXT, Japan.

The Pan-STARRS1 Surveys (PS1) and the PS1 public science archive have been made possible through contributions by the Institute for Astronomy, the University of Hawaii, the Pan-STARRS Project Office, the Max-Planck Society and its participating institutes, the Max Planck Institute for Astronomy, Heidelberg and the Max Planck In-

⁵ We use the `mag2mag` routine from Auger et al. (2009), available at <https://github.com/tcollett/LensPop/tree/master/stellarpop/>

stitute for Extraterrestrial Physics, Garching, The Johns Hopkins University, Durham University, the University of Edinburgh, the Queen's University Belfast, the Harvard-Smithsonian Center for Astrophysics, the Las Cumbres Observatory Global Telescope Network Incorporated, the National Central University of Taiwan, the Space Telescope Science Institute, the National Aeronautics and Space Administration under Grant No. NNX08AR22G issued through the Planetary Science Division of the NASA Science Mission Directorate, the National Science Foundation Grant No. AST-1238877, the University of Maryland, Eotvos Lorand University (ELTE), the Los Alamos National Laboratory, and the Gordon and Betty Moore Foundation.

Based on observations obtained as part of the VISTA Hemisphere Survey, ESO Progam, 179.A-2010 (PI: McMahon). Based on data obtained from the ESO Science Archive Facility under request number cerusu312487.

Some of the data presented herein were obtained at the W. M. Keck Observatory, which is operated as a scientific partnership among the California Institute of Technology, the University of California and the National Aeronautics and Space Administration. The Observatory was made possible by the generous financial support of the W. M. Keck Foundation.

The authors recognize and acknowledge the very significant cultural role and reverence that the summit of Mauna Kea has always had within the indigenous Hawaiian community. We are most fortunate to have the opportunity to conduct observations from this superb mountain.

REFERENCES

- Astropy Collaboration, et al., 2013, *A&A*, 558, A33
- Agnello A., Kelly B. C., Treu T., Marshall P. J., 2015, *MNRAS*, 448, 1446
- Agnello A., et al., 2017, arXiv, arXiv:1711.03971
- Agnello A., Grillo C., Jones T., Treu T., Bonamigo M., Suyu S. H., 2018, *MNRAS*, 474, 3391
- Aihara, H., Armstrong, R., Bickerton, S., et al. 2017, arXiv:1702.08449
- Auger M. W., Treu T., Bolton A. S., Gavazzi R., Koopmans L. V. E., Marshall P. J., Bundy K., Moustakas L. A., 2009, *ApJ*, 705, 1099
- Benítez N., 2000, *ApJ*, 536, 571
- Berghea C. T., Nelson G. J., Rusu C. E., Keeton C. R., Dudik R. P., 2017, *ApJ*, 844, 90
- Bertin E., Arnouts S., 1996, *A&AS*, 117, 393
- Bertin E., Mellier Y., Radovich M., Missonnier G., Didelon P., Morin B., 2002, *ASPC*, 281, 228
- Bertin E., 2006, *ASPC*, 351, 112
- Bonvin V., et al., 2017, *MNRAS*, 465, 4914
- Cardelli J. A., Clayton G. C., Mathis J. S., 1989, *ApJ*, 345, 245
- Chambers K. C., et al., 2016, arXiv, arXiv:1612.05560
- Chen G. C.-F., et al., 2016, *MNRAS*, 462, 3457
- Claeskens J.-F., Surdej J., 2002, *A&ARv*, 10, 263
- da Cunha E., et al., 2017, *PASA*, 34, e047
- de Vaucouleurs G., 1948, *AnAp*, 11, 247
- Faber S. M., Jackson R. E., 1976, *ApJ*, 204, 668
- Falco E. E., et al., 1999, *ApJ*, 523, 617
- Flaugher B., et al., 2015, *AJ*, 150, 150
- Flewelling H. A., et al., 2016, arXiv, arXiv:1612.05243
- Foreman-Mackey D., Hogg D. W., Lang D., Goodman J., 2013, *PASP*, 125, 306
- Hunter, J. D., et al. 2007, *Computing in Science & Engineering*, 9, 3, 90-95
- Jean C., Surdej J., 1998, *A&A*, 339, 729
- Keeton C. R., Kochanek C. S., Falco E. E., 1998, *ApJ*, 509, 561
- Kostrzewa-Rutkowska Z., et al., 2018, *MNRAS*
- Lee C.-H., 2017, *A&A*, 605, L8
- Lee C.-H., 2018, *MNRAS*, 475, 3086
- Lemon C. A., Auger M. W., McMahon R. G., Kuposov S. E., 2017, *MNRAS*, 472, 5023
- Lindgren L., et al., 2016, *A&A*, 595, A4
- Lucey J. R., Schechter P. L., Smith R. J., Anguita T., 2017, arXiv, arXiv:1711.02674
- Magnier E. A., et al., 2016a, arXiv, arXiv:1612.05240
- Magnier E. A., et al., 2016b, arXiv, arXiv:1612.05242
- McMahon R. G., Banerji M., Gonzalez E., Kuposov S. E., Bejar V. J., Lodieu N., Rebolo R., VHS Collaboration, 2013, *Msngr*, 154, 35
- Moffat A. F. J., 1969, *A&A*, 3, 455
- Nelder, J. A., Mead. R., 1965, *The Computer Journal* 7, 308-13
- Onaka P., Tonry J. L., Isani S., Lee A., Uyeshiro R., Rae C., Robertson L., Ching G., *Proc. 2008, Proc. SPIE*, 7014, 12
- Oguri M., et al., 2005, *ApJ*, 622, 106
- Oguri M., 2010, *PASJ*, 62, 1017
- Oguri M., Marshall P. J., 2010, *MNRAS*, 405, 2579
- Oguri M., et al., 2012, *AJ*, 143, 120
- Oliphant, T. E., 2007, *Computing in Science & Engineering*, 9, 10-20
- Ostrovski F., et al., 2018, *MNRAS*, 473, L116
- Rubin K. H. R., et al., 2017, arXiv, arXiv:1707.05873
- Rusu C. E., et al., 2016, *MNRAS*, 458, 2
- Rusu C. E., et al., 2017, *MNRAS*, 467, 4220
- Schechter P. L., Pooley D., Blackburne J. A., Wambsganss J., 2014, *ApJ*, 793, 96
- Schlafly E. F., Finkbeiner D. P., 2011, *ApJ*, 737, 103
- Secrest, N. J., Dudik, R. P., Dorland, B. N., et al. 2015, *ApJS*, 221, 12
- Shanks T., et al., 2015, *MNRAS*, 451, 4238
- Sheinis A. I., Bolte M., Epps H. W., Kibrick R. I., Miller J. S., Radovan M. V., Bigelow B. C., Sutin B. M., 2002, *PASP*, 114, 851
- Sheth, R. K., Bernardi, M., Schechter, P. L., et al. 2003, *ApJ*, 594, 225
- Skrutskie M. F., et al., 1997, *ASSL*, 210, 25
- Sluse D., Chantry V., Magain P., Courbin F., Meylan G., 2012, *A&A*, 538, A99
- Sluse D., et al., 2017, *MNRAS*, 470, 4838
- Tonry J., Onaka P. 2009, in Ryan S., ed., *Proceedings of the Advanced Maui Optical and Space Surveillance Technologies Conference. The Maui Economic Development Board, Kihei, HI*, p. E40
- Treu T., Marshall P. J., 2016, *A&ARv*, 24, 11
- Williams P., Agnello A., Treu T., 2017, *MNRAS*, 466, 3088
- Wilson M. L., Zabludoff A. I., Ammons S. M., Momcheva I. G., Williams K. A., Keeton C. R., 2016, *ApJ*, 833, 194
- Wisotzki, L., Schechter, P. L., Bradt, H. V., Heinmüller, J., & Reimers, D. 2002, *A&A*, 395, 17
- Wong K. C., et al., 2017, *MNRAS*, 465, 4895
- Wright E. L., et al., 2010, *AJ*, 140, 1868-1881
- Yonehara A., Hirashita H., Richter P., 2008, *A&A*, 478, 95
- York D. G., et al., 2000, *AJ*, 120, 1579

This paper has been typeset from a \LaTeX file prepared by the author.